Observational Properties of a Bright Type Iax SN 2018cni and a Faint Type Iax SN 2020kyg

Mridweeka Singh[1], Devendra. K. Sahu[1], Raya Dastidar[2,3], Barnabás Barna[4], Kuntal Misra[5],
Anjasha Gangopadhyay[6], D. Andrew Howell[7,8], Saurabh W. Jha[9], Hyobin Im[10,11], Kirsty Taggart[12],
Jennifer Andrews[13], Daichi Hiramatsu[7,8,14,15], Rishabh Singh Teja[1,16], Craig Pellegrino[7,8], Ryan J. Foley[17],
Arti Joshi[1], G. C. Anupama[1], K. Azalee Bostroem[18], Jamison Burke[7,8], Yssavo Camacho-Neves[9], Anirban Dutta[1,19],
Lindsey A. Kwok[9], Curtis McCully[7,8], Yen-Chen Pan[20], Matt Siebert[12], Shubham Srivastav[21], Tamás Szalai[4,22],
Jonathan J. Swift[23], Grace Yang[23], Henry Zhou[23], Nico DiLullo[23], and Jackson Scheer[23]

[1] Indian Institute of Astrophysics, Koramangala 2nd Block, Bangalore 560034, India; mridweeka.singh@iiap.res.in, yashasvi04@gmail.com
[2] Millennium Institute of Astrophysics (MAS), Nuncio Monsenor Sòtero Sanz 100, Providencia, Santiago RM, Chile
[3] Instituto de Astrofísica, Universidad Andres Bello, Fernandez Concha 700, Las Condes, Santiago RM, Chile
[4] Department of Experimental Physics, Institute of Physics, University of Szeged, H-6720 Szeged, Dóm tér 9, Hungary
[5] Aryabhatta Research Institute of observational sciencES, Manora Peak, Nainital 263 001, India
[6] Hiroshima Astrophysical Science Center, Hiroshima University, Higashi-Hiroshima, Japan
[7] Las Cumbres Observatory, 6740 Cortona Drive Suite 102, Goleta, CA 93117-5575, USA
[8] Department of Physics, University of California, Santa Barbara, CA 93106-9530, USA
[9] Department of Physics and Astronomy, Rutgers, the State University of New Jersey, 136 Frelinghuysen Road, Piscataway, NJ 08854-8019, USA
[10] Korea Astronomy and Space Science Institute, 776 Daedeokdae-ro, Yuseong-gu, Daejeon 34055, Republic of Korea
[11] Korea University of Science and Technology (UST), 217 Gajeong-ro, Yuseong-gu, Daejeon 34113, Republic of Korea
[12] Department of Astronomy and Astrophysics, University of California, Santa Cruz, CA 95064, USA
[13] Gemini Observatory, 670 North A'ohoku Place, Hilo, HI 96720-2700, USA
[14] Center for Astrophysics, Harvard & Smithsonian, 60 Garden Street, Cambridge, MA 02138-1516, USA
[15] The NSF AI Institute for Artificial Intelligence and Fundamental Interactions, USA
[16] Pondicherry University, R.V. Nagar, Kalapet, Puducherry 605014, India
[17] Department of Astronomy and Astrophysics, University of California, Santa Cruz, CA 95064-1077, USA
[18] DiRAC Institute, Department of Astronomy, University of Washington, Box 351580, U.W., Seattle, WA 98195, USA
[19] Pondicherry University, Chinna Kalapet, Kalapet, Puducherry 605014, India
[20] Graduate Institute of Astronomy, National Central University, 300 Zhongda Road, Zhongli, Taoyuan 32001, Taiwan
[21] Astrophysics Research Centre, School of Mathematics and Physics, Queen's University Belfast, Belfast BT7 1NN, UK
[22] ELKH-SZTE Stellar Astrophysics Research Group, H-6500 Baja, Szegedi út, Kt. 766, Hungary
[23] Thacher School, 5025 Thacher Road, Ojai, CA 93023-8304, USA

Abstract

We present the optical photometric and spectroscopic analysis of two Type Iax supernovae (SNe), 2018cni and 2020kyg. SN 2018cni is a bright Type Iax SN ($M_{V,\mathrm{peak}} = -17.81 \pm 0.21$ mag), whereas SN 2020kyg ($M_{V,\mathrm{peak}} = -14.52 \pm 0.21$ mag) is a faint one. We derive ^{56}Ni mass of 0.07 and 0.002 $M_\odot$ and ejecta mass of 0.48 and 0.14 $M_\odot$ for SNe 2018cni and 2020kyg, respectively. A combined study of the bright and faint Type Iax SNe in R/r-band reveals that the brighter objects tend to have a longer rise time. However, the correlation between the peak luminosity and decline rate shows that bright and faint Type Iax SNe exhibit distinct behavior. Comparison with standard deflagration models suggests that SN 2018cni is consistent with the deflagration of a CO white dwarf, whereas the properties of SN 2020kyg can be better explained by the deflagration of a hybrid CONe white dwarf. The spectral features of both the SNe point to the presence of similar chemical species but with different mass fractions. Our spectral modeling indicates stratification at the outer layers and mixed inner ejecta for both of the SNe.

Unified Astronomy Thesaurus concepts: Supernovae (1668)

Supporting material: machine-readable tables

1. Introduction

Type Ia supernovae (SNe) are the final outcome of the thermonuclear explosion of a carbon–oxygen (CO) white dwarf in a binary system (Hoyle & Fowler 1960; Wang & Han 2012; Maoz et al. 2014; Maeda & Terada 2016; Jha et al. 2019). As a group, Type Ia SNe display great uniformity and are well known as members of one parameter family (Phillips 1993;

Phillips et al. 1999). Despite the uniformity, diversity has also been noted from time to time, based on the explosion scenario (Taubenberger 2017). Among different subtypes of thermonuclear SNe, Type Iax SNe emerge as low luminosity ($M_{V,\mathrm{peak}} = -13$ to -19 mag; Jha 2017) and less energetic members (Foley et al. 2013). They are also known as 2002cx-like SNe after their prototype SN 2002cx (Li et al. 2003; Jha et al. 2006). McClelland et al. (2010) suggested a correlation between peak luminosity, the photospheric velocity at maximum, and the shape of the light curve of Type Iax SNe; however, there are a few outliers, such as SN 2009ku (Narayan et al. 2011), SN 2014ck (Tomasella et al. 2016), etc. Narayan et al. (2011) suggested a scaling relation between the decline
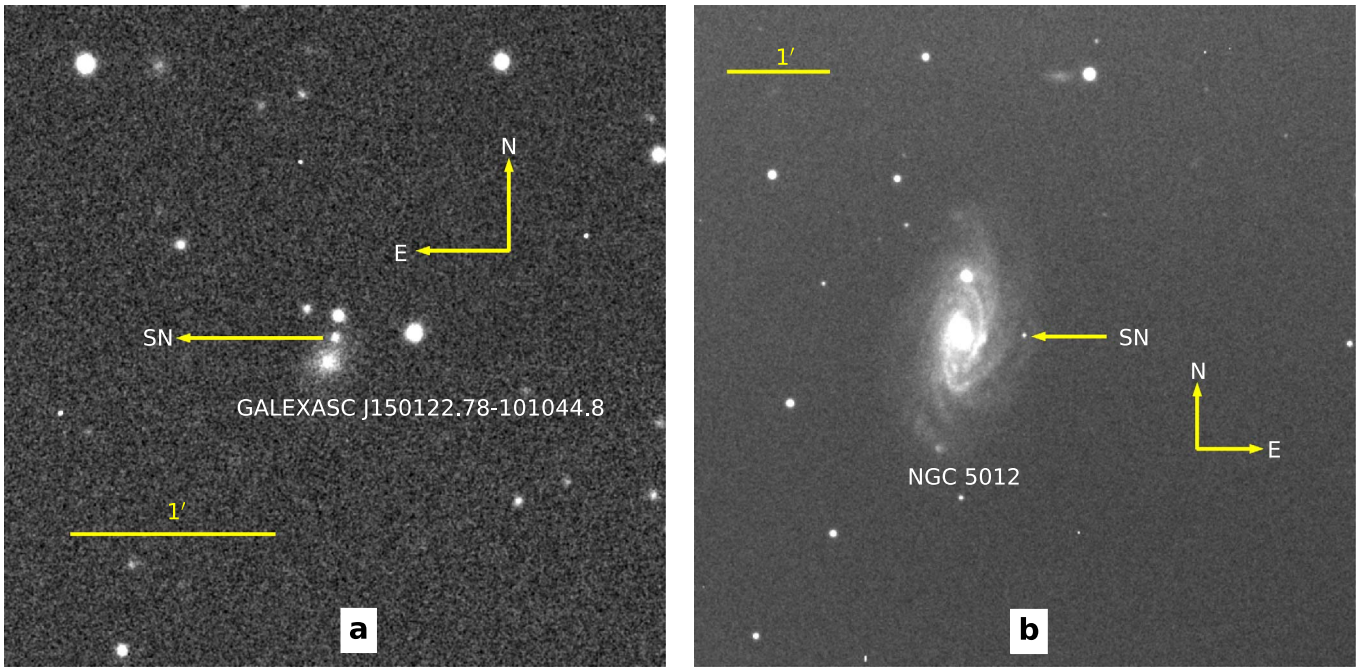
Figure 1. (a) Location of SN 2018cni in its host galaxy. This image was acquired in *V*-band with the 1 m LCO telescope on 2018 July 17. (b) SN 2020kyg and its host galaxy NGC 5012. This image was taken in *V*-band with the 1 m LCO telescope on 2020 June 27.

rate and ejecta velocity. A possible correlation between the decline rate and absolute magnitude at maximum was also shown by Foley et al. (2013) and Magee et al. (2016). The diversity in the observed properties, such as peak brightness, light curve decline rates, and ejecta velocities, indicates that Type Iax SNe form a heterogeneous class.

During the early phase, spectra of Type Iax SNe exhibit similar spectral signatures as SN 1991T-like Type Ia SNe (Phillips et al. 2007; Foley et al. 2010). They show Fe II and Fe III lines during early spectral evolution and do not display any high-velocity features (Silverman et al. 2015). The brighter Type Iax members, such as SNe 2005hk (Sahu et al. 2008), 2012Z (Stritzinger et al. 2015; Yamanaka et al. 2015), and 2020rea (Singh et al. 2022), have weaker Si II and less distinguished C II features as compared to the fainter members of this class, such as SNe 2008ha (Foley et al. 2009), 2019gsc (Srivastav et al. 2020; Tomasella et al. 2020), and 2020kyg (Srivastav et al. 2022). Furthermore, the W-shaped feature, attributed to S II (Hachinger et al. 2006), looks stronger in the spectra of the fainter Type Iax than the brighter ones.

The wide range of luminosity among members of this class presents a challenge in understanding them collectively in terms of a single physical scenario. For SN 2012Z, McCully et al. (2014a) reported the detection of a blue source coinciding with the SN location in the preexplosion images. An accreting white dwarf with a helium star in a binary system has been suggested as the plausible progenitor of SN 2012Z (McCully et al. 2014a, 2022). Jordan et al. (2012), Kromer et al. (2013), and Fink et al. (2014) proposed that the deflagration of a Chandrasekhar-mass white dwarf, leaving behind a remnant, could explain the low luminous nature of the Type Iax class. Foley et al. (2014) investigated the emission observed at the explosion site of SN 2008ha 4 yr after the explosion and discussed the possibilities of its association with the remnant of the white dwarf. Further, the presence of a bound remnant is also supported by late-time flattening found in the light curves of Type Iax SNe (McCully et al. 2014b, 2022; Singh et al. 2018; Kawabata et al. 2021). A similar explosion of a hybrid carbon–oxygen–neon (CONe) white dwarf (Meng &

Podsiadlowski 2014; Kromer et al. 2015) yields an outcome consistent with faint Type Iax SNe. Given the variety of possible progenitor channels (Pumo et al. 2009; Valenti et al. 2009; Moriya et al. 2010; Denissenkov et al. 2015; Bravo et al. 2016; Kashyap et al. 2018; Bobrick et al. 2022; Lach et al. 2022), detailed analysis of a statistically complete sample of Type Iax SNe is required to thoroughly understand the nature of this peculiar class of SNe.

Bright and faint members of the Type Iax class show diverse nature in terms of their luminosity, the synthesized mass of ^{56}Ni, spectral features, etc. This paper presents an optical follow-up of two Type Iax SNe, 2018cni and 2020kyg. SN 2018cni belongs to the bright Type Iax SNe, and SN 2020kyg is situated at the fainter end of the Type Iax class. We intend to examine the heterogeneity or homogeneity in the two extremes of luminosity distribution of Type Iax SNe. Section 2 provides information about the discovery of the SNe, observations, and reduction of the data. Distance and extinction estimations are given in Section 3. Section 4 presents a detailed description of the photometric properties of the SNe and analytical modeling of the bolometric light curve. Section 5 discusses spectroscopic properties and spectral modeling. A comparative analysis followed by a brief summary is presented in Section 6.

2. Discovery, Observation, and Data Reduction

SN 2018cni (also known as PTSS-18fdb, ATLAS18qql, and Gaia18bpu) was detected by Purple Mountain Observatory (PMO) Tsinghua Supernova Survey[24] (Tan et al. 2018) on 2018 June 13. The location of the SN is at 1″ east and 5″ south of the host galaxy GALEXASC J150122.78-101044.8. It was classified as a Type Iax SN by Zhang et al. (2018a, 2018b) using a spectrum obtained on 2018 June 17. This spectrum was found to match well with SN 2005hk, 3 days before maximum light. The location of SN 2018cni in its host galaxy is presented in Figure 1.

---

[24] PTSS, http://www.cneost.org/ptss/.

SN 2020kyg was spotted by Asteroid Terrestrial-impact Last Alert System (ATLAS; Tonry et al. 2018) at $0''.0$ north and $35''.6$ east to the center of the host galaxy NGC 5012 on 2020 May 24 (Smith et al. 2020; Tonry et al. 2020). ATLAS20nuc and AT2020kyg are other aliases of this source. A nondetection was reported on 2020 May 20 (MJD = 58989.36; Smith et al. 2020). Ochner et al. (2020) and Hiramatsu et al. (2020) classified it as a Type Iax SN before maximum. Figure 1(b) shows the position of SN 2020kyg in the host galaxy NGC 5012.

Optical photometric observations of SNe 2018cni and 2020kyg were initiated $\sim$6 and 3 days from discovery with the 1 m telescopes of the Las Cumbres Observatory (LCO; Brown et al. 2013) under the Global Supernova Project and continued up to $\sim$80 and 60 days, respectively. The photometry was performed using the `lcogtsnpipe` pipeline (Valenti et al. 2016). The *BV* magnitudes are calibrated to the Vega system, while the *gri* magnitudes are calibrated to the AB system. SN 2018cni exploded in the proximity of the host galaxy, hence template subtraction was performed in order to eliminate the host galaxy contamination. The template was observed in *BVgri* bands using the 1 m LCO telescope on 2019 August 6, which is more than a year after the discovery. The image subtraction was performed within the `lcogtsnpipe` using PyZOGY (Guevel & Hosseinzadeh 2017). The optical photometry of SNe 2018cni and 2020kyg are presented in Tables 1 and 2, respectively.

Spectroscopic observations of SNe 2018cni and 2020kyg were initiated $\sim$5 days and $\sim$1 day after the discovery, respectively. Four spectra of SN 2018cni and three spectra of SN 2020kyg were taken with FLOYDS spectrograph on the 2 m Faulkes Telescope North (FTN; Brown et al. 2013). One spectrum of SN 2018cni was acquired with the Blue Channel (BCH) spectrograph on 6.5 m MMT, and two spectra of SN 2018cni were obtained with the Robert Stobie Spectrograph (RSS) mounted on 9.2 m Southern African Large Telescope (SALT). Two spectra of SN 2018cni were obtained using the dual-beam Kast spectrograph (Miller & Stone 1993) on the Lick Shane 3 m telescope. The 300/7500 grating on the red side and the 452/3306 grism on the blue side were used, providing continuous coverage between 3500 and 10400 Å. The slit was aligned along the parallactic angle (Filippenko 1982). Two spectra of SN 2020kyg were taken with Gemini Multi-Object Spectrograph (GMOS-N) using B600 and R400 gratings on Gemini North. Spectral reduction of all spectra taken with the FLOYDS spectrograph was done using the `floydsspec`[25] pipeline. The spectrum of SN 2018cni observed with MMT was reduced using standard tasks described in Andrews et al. (2019). The two spectra from the Kast spectrograph were reduced in a standard manner using tools in a custom spectroscopy pipeline[26] (Siebert et al. 2019). The two spectra of SN 2018cni obtained from RSS were reduced using a custom pipeline that contains the PYSALT package and standard PYRAF spectral reduction tasks (Crawford et al. 2010). The Gemini spectra of SN 2020kyg were reduced using the standard Gemini IRAF package. The log of spectroscopic observations of both the SNe are provided in Tables 3 and 4, respectively.

3. Distance and Extinction

The host galaxy of SN 2018cni, GALEXASC J150122.78-101044.8, is located at a redshift of 0.032 (Zhang et al. 2018a). The extinction due to the Milky Way in the direction of SN 2018cni is $E(B-V) = 0.09$ mag (Schlafly & Finkbeiner 2011), which yields $A_V = 0.278$ mag using the Cardelli extinction law (Cardelli et al. 1989). The spectra of SN 2018cni do not exhibit significant Na ID absorption at the redshift of the host galaxy, implying negligible host extinction. SN 2020kyg is located on the outskirts of the host galaxy NGC 5012, hence noticeable extinction from the host is not expected. The extinction due to the Milky Way is $E(B-V) = 0.012$ mag (Schlafly & Finkbeiner 2011), which results in $A_V = 0.038$ mag assuming $R_v = 3.1$. We used the redshift-dependent luminosity distance for GALEXASC J150122.78-101044.8 and NGC 5012 as 130.56 ± 12.15 Mpc and 35.83 ± 2.66 Mpc, respectively (assuming $H_0 = 73$ km s^{-1} Mpc^{-1}, $\Omega_m = 0.27$, and $\Omega_v = 0.73$).

4. Light Curve Properties

4.1. Light Curve and Color Curve

Figures 2 and 3 present the light-curve evolution of SNe 2018cni and 2020kyg, respectively. Observations began before both the SNe attained peak brightness. The time and magnitude at maximum along with decline rates for both the SNe are estimated using a low-order spline fit to the light curves. The values are listed in Table 5. Light curve decline rates, $\Delta m_{15}(B)$, measured for SNe 2018cni and 2020kyg in *B*-band are 1.99 ± 0.14 mag and 2.54 ± 0.13 mag, respectively. The *I*-band light curves of SNe 2018cni and 2020kyg do not show a secondary maximum, usually seen in Type Ia SNe. Figure 4 presents the light-curve comparison of SNe 2018cni and 2020kyg in *BVRI* bands with a few well-studied Type Iax SNe 2002cx (Li et al. 2003), 2005hk (Sahu et al. 2008), 2008ha (Foley et al. 2009), 2010ae (Stritzinger et al. 2014), 2012Z (Yamanaka et al. 2015), and 2019muj (Barna et al. 2021), covering the luminosity range for this class. The *r*- and *i*-band magnitudes of SNe 2010ae, 2018cni, and 2020kyg are converted to *R*- and *I*-band using transformation equations given by Jordi et al. (2006). The magnitudes of each SN in the respective bands are normalized by their peak magnitudes. In *B*- and *V*-bands, SN 2018cni declines faster than SNe 2002cx, 2005hk, and 2012Z, while SN 2020kyg is the fastest declining SN among all the SNe used for comparison, as shown in Figure 4. In *R*- and *I*-bands, the light-curve evolution of SN 2018cni is similar to SNe 2005hk and 2012Z, while SN 2020kyg resembles SN 2008ha.

Figure 5 presents the reddening-corrected color evolution of SNe 2018cni and 2020kyg and their comparison with other well-studied Type Iax SNe. The $(B-V)$, $(V-I)$, $(V-R)$, and $(R-I)$ color evolution of SNe 2018cni and 2020kyg are found to be similar to the SNe used for comparison. This indicates that bright and faint members behave in a similar fashion in terms of color evolution.

4.2. Bolometric Light Curve and Analytical Modeling

The pseudobolometric light curves of SNe 2018cni and 2020kyg are constructed with `SuperBol` code (Nicholl 2018) in *BVri* bands using the luminosity distance discussed in Section 3. The pseudobolometric light curves of SNe 2002cx,

---

Table 1
Optical Photometric Data of SN 2018cni

Date	JD[a]	Phase[b] (days)	B (mag)	V (mag)	g (mag)	r (mag)	i (mag)
2018-06-19	288.64	−1.34	18.46 ± 0.01	18.18 ± 0.01	18.33 ± 0.01	18.13 ± 0.01	18.26 ± 0.02
2018-06-19	288.64	−1.34	18.48 ± 0.01	18.15 ± 0.01	18.32 ± 0.01	18.15 ± 0.02	18.24 ± 0.02
2018-06-20	289.98	0.00	18.35 ± 0.06	18.03 ± 0.03	18.13 ± 0.02	⋯ ± ⋯	⋯ ± ⋯
2018-06-20	290.00	0.02	⋯ ± ⋯	⋯ ± ⋯	18.22 ± 0.02	17.98 ± 0.03	18.09 ± 0.07
2018-06-20	290.00	0.02	⋯ ± ⋯	⋯ ± ⋯	⋯ ± ⋯	18.01 ± 0.03	18.12 ± 0.07
2018-06-26	295.94	5.95	18.95 ± 0.07	18.22 ± 0.08	18.78 ± 0.08	18.00 ± 0.08	18.15 ± 0.07
2018-06-26	295.94	5.95	⋯ ± ⋯	18.19 ± 0.08	18.71 ± 0.09	18.12 ± 0.07	⋯ ± ⋯
2018-06-29	298.58	8.59	19.28 ± 0.09	18.43 ± 0.04	19.13 ± 0.05	18.05 ± 0.02	18.05 ± 0.03
2018-06-29	298.58	8.59	19.42 ± 0.11	18.36 ± 0.04	19.08 ± 0.05	18.08 ± 0.02	18.09 ± 0.03
2018-07-03	303.37	13.38	20.25 ± 0.12	18.71 ± 0.04	19.58 ± 0.05	18.30 ± 0.03	18.12 ± 0.05
2018-07-03	303.38	13.39	20.04 ± 0.10	18.65 ± 0.05	19.70 ± 0.08	18.36 ± 0.03	⋯ ± ⋯
2018-07-07	306.64	16.65	20.61 ± 0.09	18.99 ± 0.04	20.10 ± 0.06	18.50 ± 0.03	18.24 ± 0.05
2018-07-07	306.64	16.65	⋯ ± ⋯	19.05 ± 0.04	20.13 ± 0.06	18.53 ± 0.03	18.39 ± 0.06
2018-07-10	309.89	19.90	20.80 ± 0.10	19.20 ± 0.03	20.43 ± 0.06	18.70 ± 0.02	18.43 ± 0.03
2018-07-10	309.89	19.90	20.86 ± 0.11	19.18 ± 0.02	20.44 ± 0.06	18.68 ± 0.02	18.41 ± 0.04
2018-07-13	312.50	22.51	21.05 ± 0.11	19.40 ± 0.05	20.74 ± 0.07	18.85 ± 0.03	18.40 ± 0.04
2018-07-13	312.50	22.51	⋯ ± ⋯	19.47 ± 0.05	20.63 ± 0.06	18.96 ± 0.03	18.46 ± 0.03
2018-07-17	317.00	27.01	20.97 ± 0.10	19.57 ± 0.06	20.64 ± 0.09	18.97 ± 0.04	18.67 ± 0.05
2018-07-17	317.00	27.01	⋯ ± ⋯	19.51 ± 0.05	20.49 ± 0.06	18.96 ± 0.04	18.75 ± 0.07
2018-07-19	319.23	29.24	21.04 ± 0.29	19.63 ± 0.14	20.69 ± 0.24	19.15 ± 0.12	18.84 ± 0.11
2018-07-19	319.23	29.24	⋯ ± ⋯	⋯ ± ⋯	20.71 ± 0.29	19.08 ± 0.11	18.86 ± 0.10
2018-07-24	323.99	34.00	⋯ ± ⋯	⋯ ± ⋯	20.56 ± 0.11	⋯ ± ⋯	18.88 ± 0.08
2018-07-24	323.99	34.00	⋯ ± ⋯	⋯ ± ⋯	⋯ ± ⋯	⋯ ± ⋯	18.83 ± 0.09
2018-07-24	324.00	34.01	⋯ ± ⋯	⋯ ± ⋯	⋯ ± ⋯	19.21 ± 0.08	18.88 ± 0.08
2018-07-24	324.00	34.01	⋯ ± ⋯	⋯ ± ⋯	⋯ ± ⋯	19.14 ± 0.08	18.83 ± 0.09
2018-07-25	325.38	35.39	⋯ ± ⋯	19.93 ± 0.27	⋯ ± ⋯	⋯ ± ⋯	⋯ ± ⋯
2018-07-27	326.88	36.89	21.08 ± 0.19	19.76 ± 0.06	⋯ ± ⋯	⋯ ± ⋯	⋯ ± ⋯
2018-07-27	326.89	36.90	⋯ ± ⋯	19.81 ± 0.09	⋯ ± ⋯	⋯ ± ⋯	⋯ ± ⋯
2018-07-27	327.38	37.39	⋯ ± ⋯	⋯ ± ⋯	21.03 ± 0.14	19.26 ± 0.07	18.85 ± 0.06
2018-07-27	327.39	37.40	⋯ ± ⋯	⋯ ± ⋯	20.97 ± 0.15	19.39 ± 0.10	⋯ ± ⋯
2018-07-29	328.57	38.58	21.02 ± 0.43	⋯ ± ⋯	⋯ ± ⋯	⋯ ± ⋯	⋯ ± ⋯
2018-07-29	328.57	38.58	⋯ ± ⋯	19.86 ± 0.28	⋯ ± ⋯	⋯ ± ⋯	⋯ ± ⋯
2018-07-29	329.46	39.47	⋯ ± ⋯	⋯ ± ⋯	20.97 ± 0.14	19.52 ± 0.06	19.26 ± 0.09
2018-07-29	329.46	39.47	⋯ ± ⋯	⋯ ± ⋯	⋯ ± ⋯	19.50 ± 0.07	19.29 ± 0.10
2018-08-04	334.97	44.98	21.28 ± 0.20	19.91 ± 0.07	20.94 ± 0.13	19.48 ± 0.06	19.27 ± 0.11
2018-08-04	334.97	44.98	21.26 ± 0.17	19.87 ± 0.06	20.98 ± 0.15	19.35 ± 0.07	19.29 ± 0.10
2018-08-10	340.56	50.57	21.57 ± 0.18	20.11 ± 0.08	20.95 ± 0.13	19.72 ± 0.06	19.39 ± 0.06
2018-08-10	340.57	50.58	⋯ ± ⋯	20.12 ± 0.08	21.02 ± 0.12	19.71 ± 0.05	19.56 ± 0.09
2018-08-20	350.54	60.55	⋯ ± ⋯	20.11 ± 0.09	20.85 ± 0.11	19.83 ± 0.09	19.77 ± 0.13
2018-08-22	352.51	62.52	21.43 ± 0.48	20.32 ± 0.19	20.78 ± 0.30	19.79 ± 0.12	19.77 ± 0.18
2018-08-22	352.52	62.53	⋯ ± ⋯	⋯ ± ⋯	20.75 ± 0.26	⋯ ± ⋯	⋯ ± ⋯
2018-08-31	362.22	72.23	⋯ ± ⋯	20.30 ± 0.11	21.31 ± 0.14	20.25 ± 0.10	19.79 ± 0.17

Notes.

[a] JD 2,458,000+.

[b] Phase has been calculated with respect to $B_{max} = 2458289.99$.

(This table is available in machine-readable form.)

2005hk, 2008ha, and 2010ae are constructed in a similar manner and are presented in Figure 6. We find that the bolometric luminosity of SN 2018cni is similar to bright Type Iax SN 2005hk, whereas SN 2020kyg lies between SNe 2008ha and 2010ae and belongs to the fainter class of Type Iax SNe. We have also used the SuperBol code to calculate the *BgVri* luminosities of SNe 2018cni and 2020kyg, which are shown in Figure 7.

Explosion parameters of both the SNe are estimated using Arnett's model (Arnett 1982) along with the formulation given in Valenti et al. (2008). Homologous expansion, spherically symmetric ejecta, no mixing of ^{56}Ni, and optically thick ejecta are basic assumptions used in the model. The mass of ^{56}Ni and the timescale of the light curve (τ) are free parameters for the fitting. Optical opacity is fixed to 0.07 cm^2 g^{-1} and photospheric velocities used are 7000 km s^{-1} and 4500 km s^{-1} (Section 5.1) for SNe 2018cni and 2020kyg, respectively.

Analytical modeling of the pseudobolometric light curve of SN 2018cni gives a mass of ^{56}Ni $\sim 0.07 \pm 0.01 M_{\odot}$ and the ejecta a mass of 0.48 $M_{\odot}$. For SN 2020kyg, these estimates are a mass of ^{56}Ni $\sim 0.002 \pm 0.001$ $M_{\odot}$ and an ejecta mass of 0.14 $M_{\odot}$. For SN 2020kyg, our estimated values are lower than that presented in Srivastav et al. (2022), where *ugrizyJHK* fluxes were used for estimating the explosion parameters. The evolution of the blackbody temperature and radius for SNe 2018cni and 2020kyg are shown in Figure 8. Despite the large difference in luminosity for the two SNe, their blackbody-temperature evolution is similar, whereas the blackbody radius

Table 2
Optical Photometric Data of SN 2020kyg

Date	JD[a]	Phase[b] (days)	B (mag)	V (mag)	g (mag)	r (mag)	i (mag)
2020-05-27	996.88	−2.05	18.54 ± 0.22	18.28 ± 0.14	18.38 ± 0.04	18.34 ± 0.03	18.55 ± 0.03
2020-05-29	998.94	0.00	18.36 ± 0.06	18.28 ± 0.05	18.37 ± 0.01	18.35 ± 0.02	18.48 ± 0.03
2020-05-31	1000.92	1.98	18.56 ± 0.06	18.36 ± 0.06	18.48 ± 0.02	18.31 ± 0.03	18.38 ± 0.04
2020-06-01	1002.34	3.40	18.83 ± 0.10	18.42 ± 0.09	18.74 ± 0.06	18.36 ± 0.05	18.42 ± 0.07
2020-06-05	1006.28	7.34	19.91 ± 0.22	18.63 ± 0.08	19.20 ± 0.06	18.47 ± 0.04	18.48 ± 0.04
2020-06-09	1010.21	11.27	20.69 ± 0.11	19.17 ± 0.06	20.07 ± 0.05	18.76 ± 0.02	18.65 ± 0.03
2020-06-15	1016.28	17.34	21.02 ± 0.10	19.63 ± 0.06	⋯ ± ⋯	19.19 ± 0.02	19.05 ± 0.04
2020-06-15	1016.28	17.34	21.14 ± 0.12	19.54 ± 0.06	⋯ ± ⋯	19.24 ± 0.02	19.12 ± 0.04
2020-06-15	1016.80	17.86	⋯ ± ⋯	19.59 ± 0.06	⋯ ± ⋯	⋯ ± ⋯	⋯ ± ⋯
2020-06-16	1016.91	17.97	⋯ ± ⋯	19.56 ± 0.10	20.28 ± 0.03	19.13 ± 0.01	18.93 ± 0.01
2020-06-19	1019.83	20.89	20.76 ± 0.22	20.04 ± 0.15	⋯ ± ⋯	⋯ ± ⋯	⋯ ± ⋯
2020-06-22	1023.21	24.27	21.39 ± 0.14	20.09 ± 0.07	⋯ ± ⋯	19.67 ± 0.03	19.37 ± 0.04
2020-06-22	1023.22	24.28	⋯ ± ⋯	20.03 ± 0.07	⋯ ± ⋯	19.57 ± 0.03	19.43 ± 0.05
2020-06-27	1027.85	28.91	21.59 ± 0.37	20.38 ± 0.09	21.24 ± 0.11	19.91 ± 0.06	19.61 ± 0.05
2020-06-27	1027.85	28.91	21.64 ± 0.32	20.11 ± 0.09	21.81 ± 0.20	19.84 ± 0.04	19.81 ± 0.07
2020-07-01	1032.21	33.27	⋯ ± ⋯	20.43 ± 0.17	21.26 ± 0.20	20.09 ± 0.11	19.74 ± 0.10
2020-07-01	1032.21	33.27	⋯ ± ⋯	20.62 ± 0.22	21.75 ± 0.43	19.94 ± 0.07	⋯ ± ⋯
2020-07-06	1037.22	38.28	⋯ ± ⋯	20.67 ± 0.17	21.62 ± 0.31	20.40 ± 0.12	20.00 ± 0.13
2020-07-06	1037.22	38.28	⋯ ± ⋯	20.89 ± 0.24	⋯ ± ⋯	20.03 ± 0.07	⋯ ± ⋯
2020-07-12	1043.21	44.27	⋯ ± ⋯	21.66 ± 0.36	⋯ ± ⋯	20.25 ± 0.33	— ± −
2020-07-15	1045.87	46.93	⋯ ± ⋯	21.65 ± 0.23	⋯ ± ⋯	21.59 ± 0.24	20.11 ± 0.13
2020-07-22	1053.20	54.26	⋯ ± ⋯	21.32 ± 0.24	⋯ ± ⋯	20.96 ± 0.14	20.54 ± 0.11

Notes.
[a] JD 2,458,000+.
[b] Phase has been calculated with respect to $B_{max} = 2458998.94$.

(This table is available in machine-readable form.)

**Table 3**
Log of Spectroscopic Observations for SN 2018cni

Date	JD[a]	Phase[b] (days)	Spectral Range (Å)	Resolution	Telescope/Instrument
2018-06-18	287.79	−2.2	3300–11000	400–700	FTN/FLOYDS
2018-06-19	288.76	−1.2	3500–10400	400	SHANE/Kast
2018-06-29	298.81	8.8	3300–11000	400–700	FTN/FLOYDS
2018-07-05	304.14	14.2	3900–6800	3900	MMT/BCH
2018-07-11	311.35	21.4	3500–9300	1000	SALT/RSS
2018-07-20	319.72	29.7	5620–10400	400	SHANE/Kast
2018-07-24	323.99	34.0	3200–11000	400–700	FTN/FLOYDS
2018-07-26	325.98	35.9	3200–11000	400–700	FTN/FLOYDS
2018-08-14	345.26	55.3	3500–9300	1000	SALT/RSS

Notes.
[a] 2,458,000+.
[b] Phase has been calculated with respect to $B_{max} = 2458289.99$.

Table 4
Log of Spectroscopic Observations for SN 2020kyg

Date	JD[a]	Phase[b] (days)	Spectral Range (Å)	Resolution	Telescope/Instrument
2020-05-25	994.93	−4.0	3300–11000	400–700	FTN/FLOYDS
2020-05-26	995.80	−3.1	3200–10000	400–700	FTN/FLOYDS
2020-06-04	1004.85	5.9	3200–10000	400–700	FTN/FLOYDS
2020-06-14	1014.81	15.8	4000–9000	1688,1900	Gemini/GMOS-N
2020-07-03	1033.83	34.9	4000–9000	1688,1900	Gemini/GMOS-N

Notes.
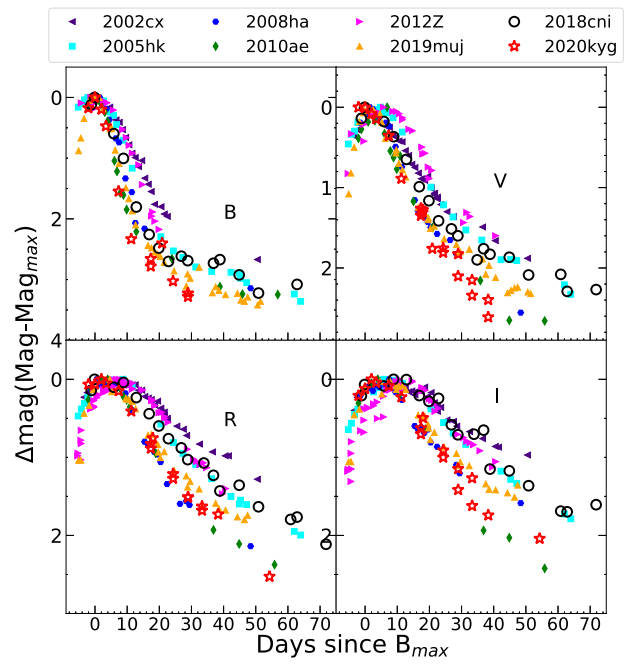[a] 2,458,000+.
[b] Phase is from $B_{max} = 2458998.94$.
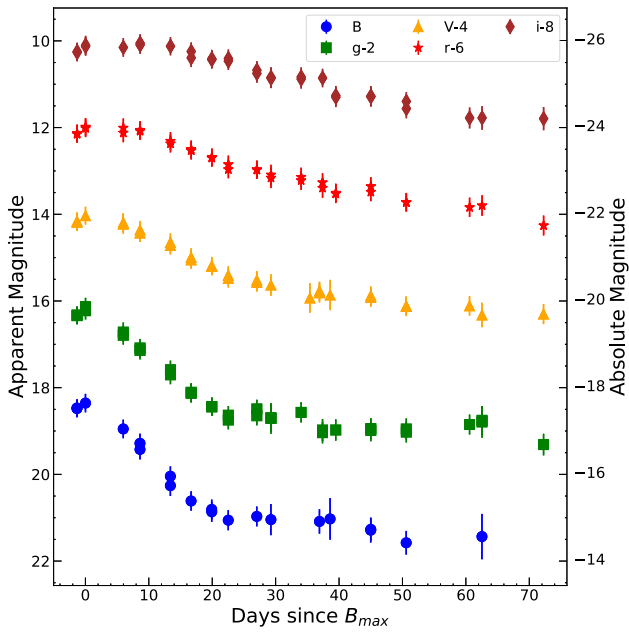
Figure 2. This figure shows the light-curve evolution of SN 2018cni in *BgVri* bands. In the right *Y*-axis, absolute magnitudes in the corresponding *BgVri* bands are presented.
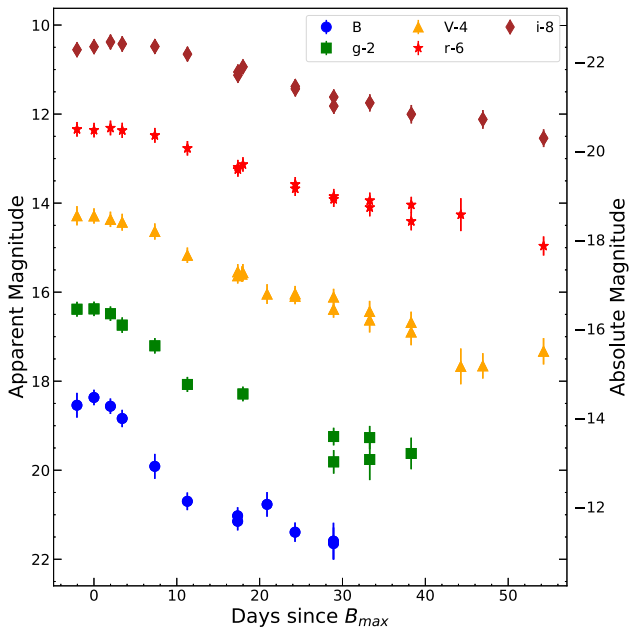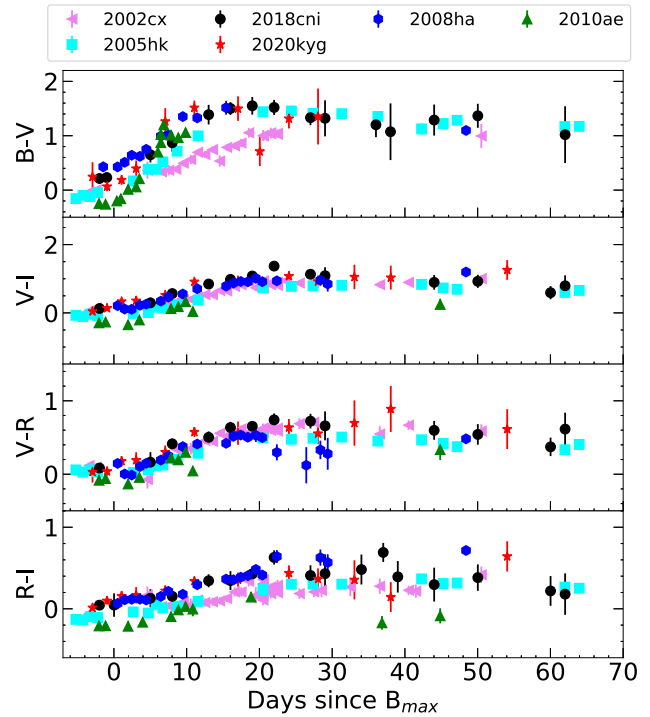

Figure 3. Light-curve evolution of SN 2020kyg in *BgVri* bands. Absolute magnitudes in *BgVri* bands for SN 2020kyg are shown on the right *Y*-axis.

Figure 4. Comparison of the normalized light curves of SNe 2018cni and 2020kyg with a few other well-studied Type Iax SNe.
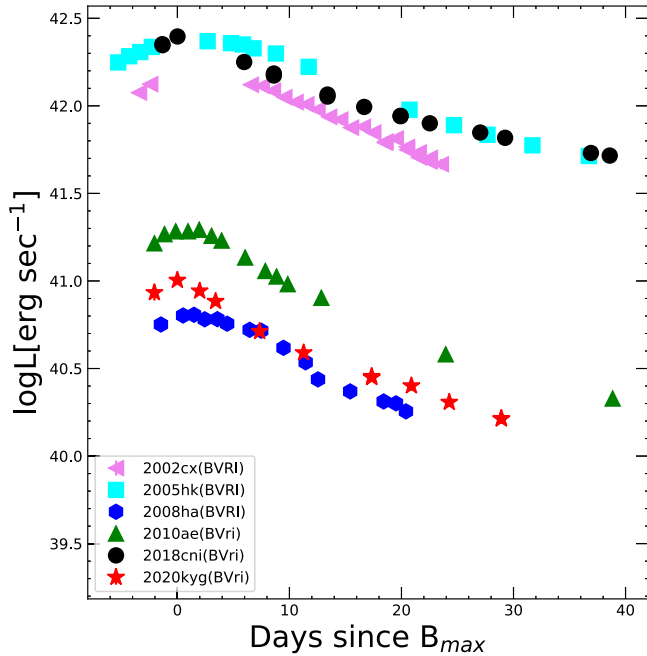

Figure 5. Color curves of SNe 2018cni and 2020kyg and their comparison with the color evolution of other Type Iax SNe.

is larger for the bright SN 2018cni. This suggests that diversity in luminosity is directly related to the radius of the photosphere, which, in turn, is related to expansion velocity.

Because of the intrinsic heterogeneity of SNe Iax, the contribution of UV and near-infrared (NIR) flux to the bolometric flux is not well constrained. However, depending on the availability of the data in UV and NIR bands, the fractional contribution of UV and NIR flux to the bolometric flux has been reported for a number of SNe Iax. For SN 2005hk, Phillips et al. (2007) estimated a 20% contribution of UV flux to the UVOIR light curve at the early time of evolution. Yamanaka et al. (2015) showed that the NIR band

contributes ∼20% to Opt+NIR around the maximum for SN 2012Z. A total UV+IR contribution of ∼35% has been reported for SN 2014ck (Tomasella et al. 2016). Srivastav et al. (2020) and Dutta et al. (2022) quoted the ratio of peak quasi-bolometric luminosity to peak blackbody bolometric luminosity as 0.69 (SN 2019gsc) and 0.62 (SN 2020sck), respectively. For SN 2020kyg, Srivastav et al. (2022) estimated a 60% contribution from the optical luminosity to the total bolometric luminosity around the maximum. If ∼35% flux is added to the

Table 5
Parameters of SNe 2018cni and 2020kyg

SN 2018cni	B-band	V-band	g-band	r-band	i-band
JD of maximum light (2458000+)	289.99 ± 0.5	289.99 ± 0.5	289.99 ± 0.5	290.00 ± 0.5	290.01 ± 0.5
Magnitude at maximum (mag)	18.36 ± 0.07	18.03 ± 0.04	18.13 ± 0.02	17.98 ± 0.03	18.09 ± 0.08
Absolute magnitude at maximum (mag)	−17.59 ± 0.21	−17.81 ± 0.21	−17.78 ± 0.20	−17.82 ± 0.20	−17.65 ± 0.22
Δm_{15}(mag)	1.99 ± 0.14	0.79 ± 0.07	1.61 ± 0.09	0.48 ± 0.06	0.18 ± 0.08
SN 2020kyg					
JD of maximum light (2458000+)	998.94 ± 2.0	996.88 ± 0.5	998.95 ± 2	1000.9 ± 0.5	1000.9 ± 0.5
Magnitude at maximum (mag)	18.36 ± 0.06	18.28 ± 0.14	18.37 ± 0.02	18.31 ± 0.03	18.38 ± 0.04
Absolute magnitude at maximum (mag)	−14.45 ± 0.17	−14.52 ± 0.21	−14.44 ± 0.16	−14.49 ± 0.16	−14.41 ± 0.17
Δm_{15}(mag)	2.54 ± 0.13	0.98 ± 0.19	1.77 ± 0.08	0.84 ± 0.06	0.61 ± 0.06

Figure 6. This figure presents the pseudobolometric light curves of SNe 2018cni and 2020kyg. The pseudobolometric light curves of SNe 2002cx, 2005hk, 2008ha, and 2010ae are included for comparison. The figure shows that SN 2018cni belongs to the bright Type Iax SNe, whereas SN 2020kyg conforms to the fainter class of Type Iax SNe.

Figure 7. Pseudobolometric light curves of SNe 2018cni and 2020kyg obtained through `SuperBol` along with their respective Arnett–Valenti model (dashed line) fits.

pseudobolometric flux of SNe 2018cni and 2020kyg, the mass of ^{56}Ni increases to 0.09 $M_\odot$ and 0.003 $M_\odot$, respectively. In this study, we have used pseudobolometric fluxes and reported the lower limit for the explosion parameters.

We compare the *BgVri* bolometric light curves of SNe 2018cni and 2020kyg with model light curves of deflagration of a CO white dwarf (Fink et al. 2014) and a hybrid CONe white dwarf (Kromer et al. 2015), respectively, in Figure 9. These model light curves are taken from the HESMA database. In the model light curves of CO white dwarfs, N1-def, N3-def, N5-def, and N10-def correspond to 1, 3, 5, and 10 ignition spots, respectively. The increasing number of ignition spots indicates a stronger explosion. We find that SN 2018cni is similar to the N3-def model and the low-luminosity SN 2020kyg is better explained by the deflagration of the CONe white dwarf. Since the models used for comparison include flux from UV to NIR and we have only *BgVri* fluxes, we intend to only investigate the probable explosion scenario by finding the

best match between the theoretical models and the observed luminosity of both the SNe.
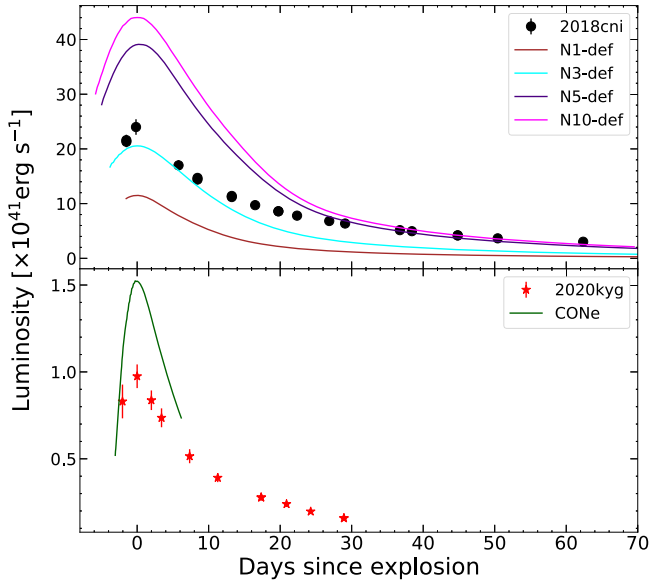
5. Prime Spectral Features

5.1. Spectral Features and Comparison with Other SNe

Figures 10 and 11 show the spectral sequence of SNe 2018cni and 2020kyg from −2 days to +55 days and −4.0 days to +35 days with respect to the maximum in the B-band, respectively. The first spectrum of SN 2018cni at −2 days shows a blue continuum with Ca II H&K, Fe III, and Si III lines, while beyond 5200 Å, the spectrum is featureless. In the postmaximum phase, the continuum in the blue region weakens. The postmaximum spectra of SN 2018cni exhibit Fe II features near 5000 Å, Co II features near 6500 Å, and Ca II NIR features. Spectra of SN 2018cni are compared with spectra of SNe 2002cx (Li et al. 2003) and 2005hk (Sahu et al. 2008), at comparable epochs in Figure 12. In the premaximum phase (top panel), the strength of the Fe III λ4420 line appears to be similar in all three SNe, while the Si III λ4553, 4568 lines in SN 2018cni appear stronger than the other two SNe. During the postmaximum epoch (middle and bottom panel), spectra of SN
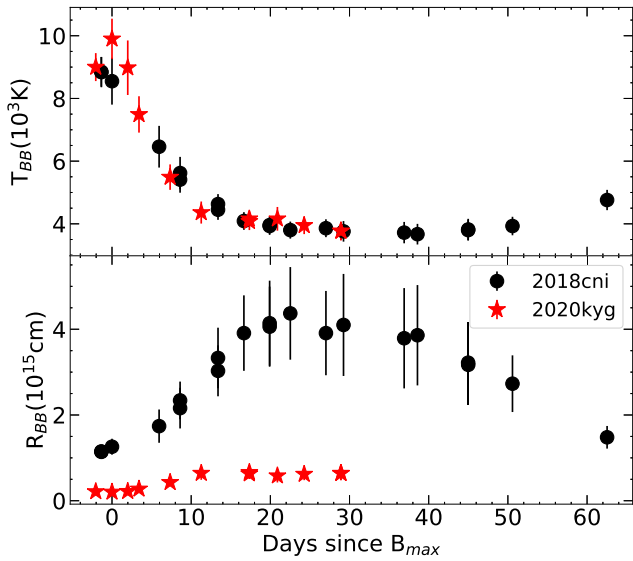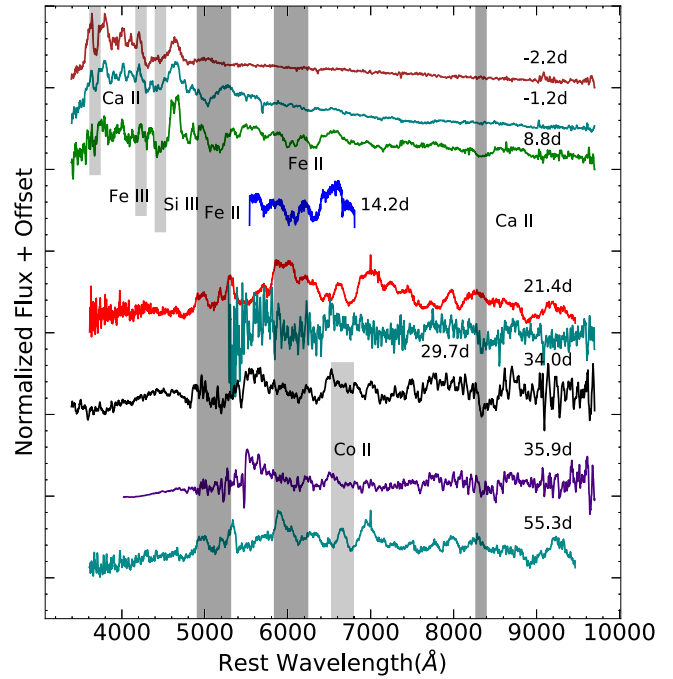
Figure 8. This figure depicts the evolution of blackbody temperature and radius obtained through `SuperBol`. The evolution of the blackbody temperature is the same for both SNe, whereas the blackbody radius is higher for SN 2018cni than SN 2020kyg.
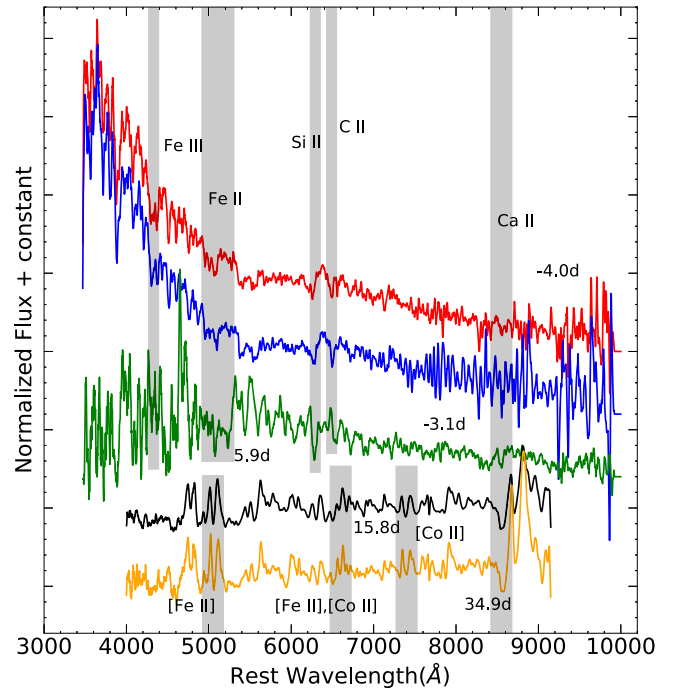

Figure 10. Spectral evolution of SN 2018cni from −2 to 55 days since maximum.

Figure 9. Comparison of the bolometric light curves of different proposed models with the pseudobolometric light curves of SNe 2018cni and 2020kyg.

Figure 11. Spectral sequence of SN 2020kyg at −4.0, −3.1, 5.9, 15.8, and 34.9 days since maximum.

2018cni are dominated by iron group elements (IGE) and display a good one-to-one correspondence in the spectral features with SNe 2002cx and 2005hk.

In the spectral evolution of SN 2020kyg, narrow P-Cygni profiles of intermediate-mass elements (IMEs) and IGEs are present. In Figure 12(b), we compare the spectra of SN 2020kyg with other faint Type Iax SNe 2008ha (Foley et al. 2009), 2010ae (Stritzinger et al. 2014), and 2019gsc (Srivastav et al. 2020). In the premaximum phase, strong features due to C II and Si II can be seen in all the spectra. The presence of C II is indicative of unburnt carbon in the progenitor system. In the early postmaximum phase, C II and Si II lines become weak, and Fe II around 5000 Å can be seen with almost equal strength in spectra of SN 2020kyg and other

SNe used for comparison. In the postmaximum phase, the Ca II NIR feature starts developing in all of the SNe. An overall similarity can be seen in the spectral signatures of SN 2020kyg with other SNe used for comparison. Spectra of SN 2020kyg at +16 and +35 days are very similar, mainly dominated by permitted and forbidden lines due to Fe II, Co II, and Ca II. The presence of forbidden lines in the +16 days spectrum indicates a considerably fast evolution of SN 2020kyg and its early transition into the nebular phase.
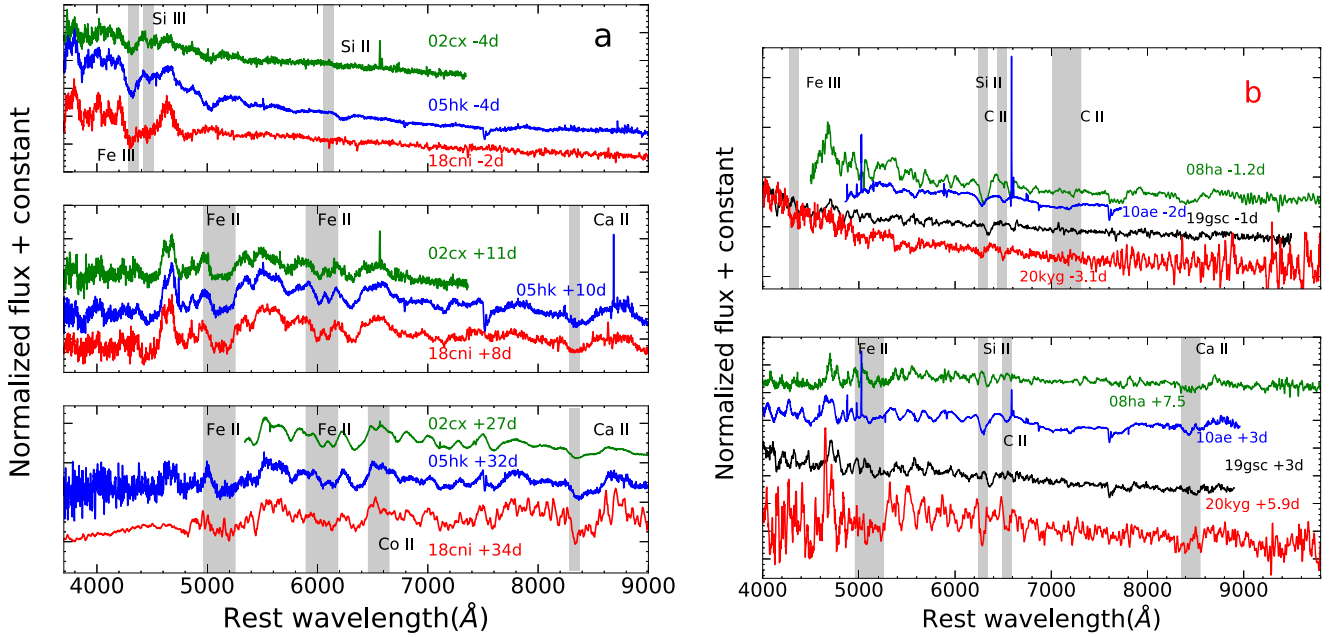
Figure 12. (a) This figure represents the comparison between spectra of SNe 2018cni, 2002cx, and 2005hk. (b) This figure shows the comparison between the spectra of SNe 2020kyg, 2008ha, 2010ae, and 2019gsc. The comparison features in both figures are marked with shaded bars.

We measure the expansion velocity of SN 2020kyg by fitting a Gaussian function to the absorption minima of the Si II profile. The estimated velocities at three epochs (-4.0, -3.1, and $+5.9$ days) are 4330, 4290, and 3580 km s^{-1}, respectively. The measurement errors associated with the estimation of expansion velocities are $\sim$600 km s^{-1}. Our estimations are consistent with the values given in Srivastav et al. (2022). As the identification of the Si II line in SN 2018cni is questionable, we did not attempt to measure its expansion velocity.

5.2. Spectral Modeling

We perform spectral modeling for SN 2018cni at three epochs and SN 2020kyg at four epochs (Figures 13 and 14) using the one-dimensional radiative transfer code TARDIS (Kerzendorf & Sim 2014; Kerzendorf et al. 2018). TARDIS assumes a blackbody-emitting photosphere with a custom-designed, spherically symmetric ejecta. The one-dimensional density and abundance structure was the subject of fitting, following the abundance tomography method described in Barna et al. (2018): as the homologously expanding SN ejecta becomes optically thinner, the velocity of the photosphere decreases and observations can probe deeper into the ejecta.

The assumed density function is designed to resemble those of the various pure deflagration models (Fink et al. 2014), similar to previous attempts of fitting SN Iax spectra (Barna et al. 2021). This density function includes a simple exponential inner and a more strongly decreasing outer part:

$$\rho(v, t_{\exp}) = \begin{cases} \rho_0 \cdot \left(\dfrac{t_{\exp}}{t_0}\right)^{-3} \cdot \exp\left(-\dfrac{v}{v_0}\right) & \text{for } v \leqslant v_{\text{cut}} \\[2ex] \rho_0 \cdot \left(\dfrac{t_{\exp}}{t_0}\right)^{-3} \cdot \exp\left(-\dfrac{v}{v_0}\right) \cdot 8^{-\frac{8(v-v_{\text{cut}})^2}{v_{\text{cut}}^2}} & \text{for } v > v_{\text{cut}} \end{cases},$$

(1)
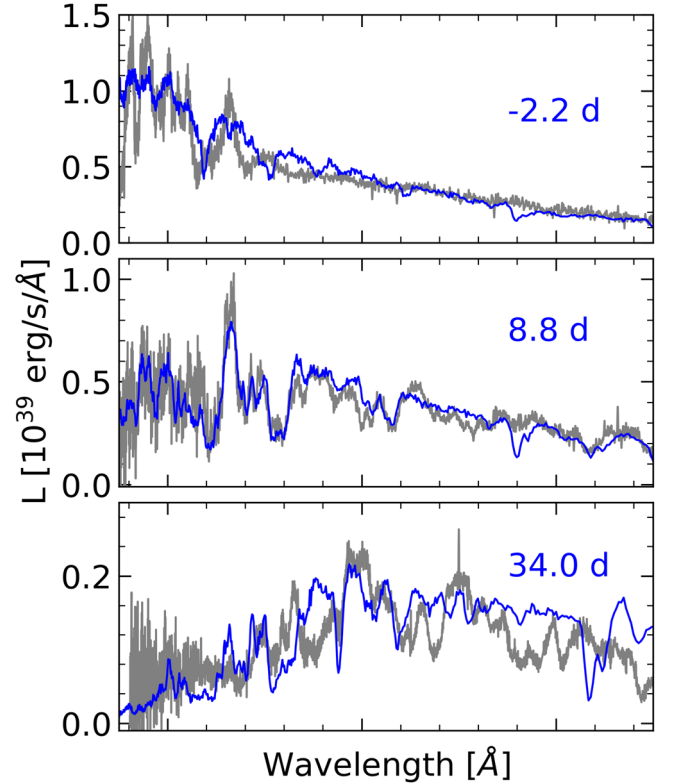
Figure 13. This figure presents the spectral fitting of SN 2018cni using TARDIS. The gray and blue lines show the SN spectra and the corresponding models, respectively.

where the innermost density ρ_0 (at reference time $t_0 = 100$ s), the slope of the function v_0, and the start of the shallow cutoff past the velocity v_{cut} are free parameters in the fitting process.

Abundances are constrained by fitting the prominent P-Cygni features at all spectral epochs of the actual SN, simultaneously. The model ejecta is split into 1000 km s^{-1}
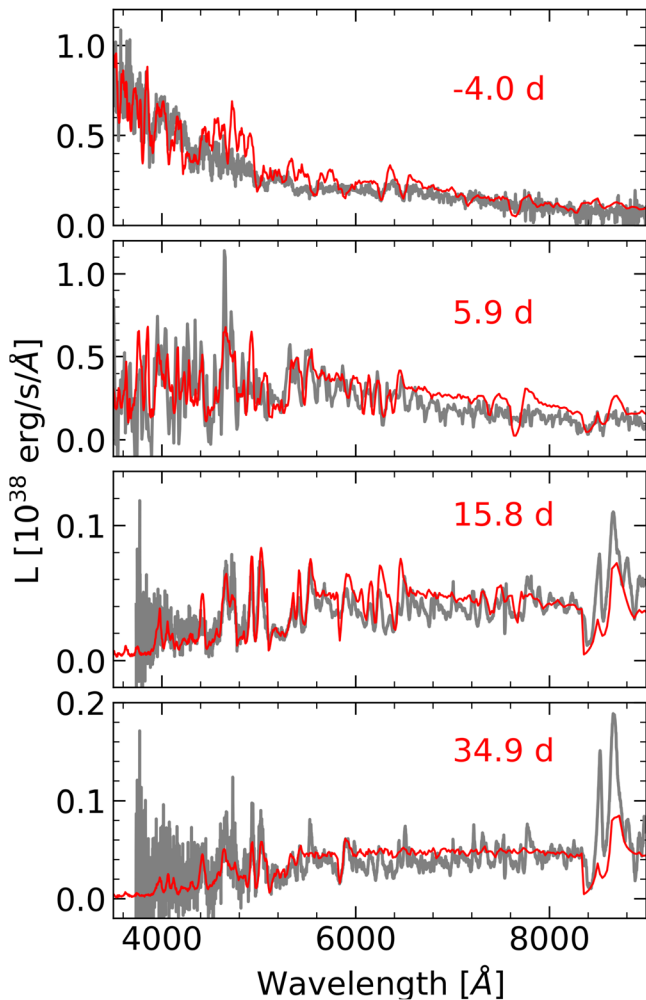
Figure 14. Fitting of the spectra of SN 2020kyg using TARDIS is shown in this figure. Here, gray lines display the spectra of the SN and red lines present the respective models.

Table 6
Parameters of the Best-fit Models of SNe 2018cni and 2020kyg from Our Spectral Synthesis Method

	SN 2018cni	SN 2020kyg
Δt [days]	16	10.8
v_{max} [km s^{-1}]	7500	3100
Core density [g cm^{-3}]	1.40	0.15
Density slope [km s^{-1}]	2700	2800
Cutoff velocity [km s^{-1}]	7000	...

Notes. Δt and v_{max} represent t_{exp} and v_{phot} at maximum light. Assuming an epoch of maximum light $B_{max} = 2458289.99$ and 2458998.94 JD for SNe 2018cni and 2020kyg, respectively.

zones, where the mass fractions of the prominent chemical elements are fitting parameters.

Due to the high number of mass fraction parameters, the whole parameter space cannot be fully explored manually. Thus, a different combination of physical and chemical properties, which would provide a similarly good match with the observed spectra, cannot be fully ruled out. However, considering that the main spectral features and the flux continuum of each epoch are well reproduced, we conclude that our results provide at least feasible solutions.

Other input parameters are the luminosity and the time since the explosion. The latter parameter controls the dilution of the density structure, and thus, affects the estimated temperature profile of the model ejecta. In the absence of good photometric coverage during the early phase, the explosion date is constrained from the spectral synthesis, as t_{exp} has a critical impact on the premaximum epochs. The best-fit date is considered as the date of the explosion. In the case of SN 2020kyg, the inferred date of the explosion is in agreement with that of Srivastav et al. (2022; JD = 2458988.3), within the estimated ± 1.0 day uncertainty. The explosion epoch for SN 2018cni estimated in a similar manner is JD = 2458275.3. Luminosities are measured from the bolometric light curve,

allowing variation within the uncertainty range of the bolometric estimations.

The main parameters of the best-fit model structures for SNe 2018cni and 2020kyg can be found in Table 6. The two objects fit in the general trend of other SNe Iax studied by abundance tomography, which displays increasing ejecta mass and rise time with luminosity. The constrained density functions (Figures 15 and 16) exhibit a relatively good agreement with the predictions of the pure deflagration models with corresponding luminosities.

Srivastav et al. (2022) fitted a different subset of the spectral time series of SN 2020kyg, following the same principles of the abundance tomography technique and the same radiative transfer code. The density functions show nearly the same profile with a slope of $v_0 = 2800$ km s^{-1} (3000 km s^{-1} in Srivastav et al. 2022), which is the key parameter in reproducing the observed P-Cygni features. The model of Srivastav et al. (2022) also has a slightly lower core density of $\rho_0 = 0.03$ g cm^{-3}. As a significant difference, our model fitting constrained lower v_{phot} velocities over the epochs (assuming a linear decrease with time): for the only epoch included in both samples ($t_{exp} = 6.5$ days), we derived $v_{phot} = 3500$ km s^{-1} instead of 4200 km s^{-1}, which results in a hotter photosphere. The source of discrepancy is in the different characterization of the temperature profile, which also greatly affects the inferred chemical abundances. In the nearly uniform chemical structure of Srivastav et al. (2022), carbon is the dominant element ($X(C) = 0.60$) with significant contributions of O and minor abundances of Si, Fe, and ^{56}Ni. Note that such an extreme abundance of C is in conflict with the plausible explosion scenarios.

In this study, we aimed to constrain the abundance structure by adopting the general characteristics of the pure deflagration models (Fink et al. 2014; Lach et al. 2022) as a starting point for our fitting process. The final results are plotted in Figures 15 and 16. The outer layers of the models are dominated by C and O, suggesting that not the entire ejecta was reached by the fusion flame. At lower velocities, O is still the most abundant element in the entire regime of our models, while carbon is excluded from the inner regions (the lower limit is 10,000 km s^{-1} for SN 2018cni and 4000 km s^{-1} for SN 2020kyg), otherwise, the C II lines would be extreme around the maximum light. These results strongly contradict the predictions of the pure deflagration scenario, but one should treat them with caution: O is also used as a puffer element to fill the unconstrained mass fractions; thus, $X(O)$ is highly uncertain.
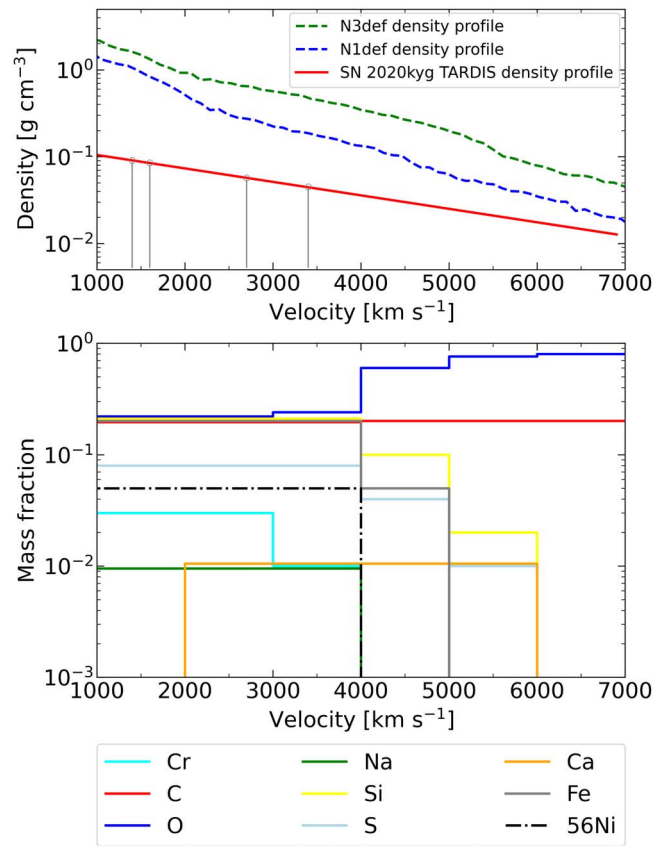
In general, the chemical distribution of the inner structure (i.e., below the carbon-populated layers) resembles the
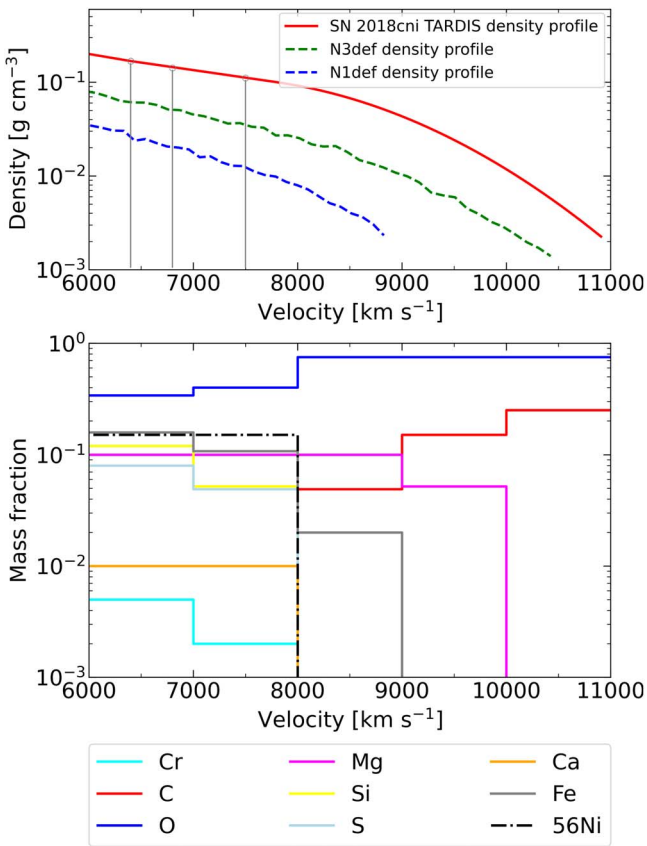
Figure 15. Top panel: the best-fit function for SN 2018cni (red) compared to the N1-def and N3-def pure deflagration density structure at $t_{exp} = t_0 = 100$ s. The gray lines indicate the boundaries of the fitting layers for the corresponding chemical abundance models. Bottom panel: the best-fit chemical abundance structure from the TARDIS fitting process for the spectral sequence of SN 2018cni. The profile of the radioactive ^{56}Ni shows the mass fractions at $t_{exp} = 100$ s.

Figure 16. Same as in Figure 15 but for SN 2020kyg.

predictions of the pure deflagration models (Fink et al. 2014), as the elements forming the dominant spectral features (O, Si, S, Fe, and Ni) show nearly constant abundances. The total IGE mass fraction is lower than expected (X(IGE) ~ 0.55 for N1-def and N3-def models), which is the consequence of the weakly constrained $X(^{56}$Ni). Despite the significantly lower densities of the outer regions adopted in our approach, Si, S, Fe, and Ni are either absent or present only with a significantly lower mass fraction. Magee et al. (2022) argued for strong mixing and uniform abundances, but their work was limited to the analysis of a few lines instead of fitting the whole optical wavelength range and studying a stratification model fixed to the radial coordinates. However, this study, just like previous fitting approaches, does not contradict the results of Magee et al. (2022), that the inner regions may inhibit a nearly uniform abundance structure.

Moreover, the complete lack of or very low abundances of IMEs and IGEs in the outer regions are relatively well constrained in our models by the blue wings of absorption features, and further supported by the low-density values at these higher velocities. This result indeed indicates some level of stratification; however, not necessarily a continuously changing multilayer structure. Instead, a C/O-dominated top layer with a deflagration-like well-mixed ejecta is also supported by the spectral synthesis.

6. Discussion and Summary

This paper presents a combined analysis of a bright Type Iax SN 2018cni and a faint Type Iax SN 2020kyg. We attempted to comprehend the nature of the members of the Type Iax class, which are located at the two extremes in the luminosity space of this class. We see that in terms of photometric properties, spectral features, and ejecta configuration these two SNe behave differently. This also reflects that there might be a difference in the progenitor channels for both events. In the following, we summarize our findings for both events and try to make a collective picture of these two events as members of the same class with a gap in luminosity distribution.

SN 2018cni is a bright member of the Type Iax class with peak absolute magnitude $M_V = -17.81 \pm 0.21$ mag. The estimated bolometric luminosity shows that SN 2018cni shares a similarity with SN 2005hk and is brighter than SN 2002cx. The mass of ^{56}Ni estimated from the analytical modeling of the $BgVri$ bolometric light curve is $\sim 0.07 \pm 0.01$ $M_\odot$. The spectral features of SN 2018cni match well with SNe 2002cx and 2005hk.

With peak absolute magnitude, $M_g = -14.44 \pm 0.16$ mag, SN 2020kyg lies at the fainter end of Type Iax luminosity distribution. It is brighter than SNe 2008ha (Stritzinger et al. 2014), 2019gsc (Srivastav et al. 2020), and 2021fcg (Karambelkar et al. 2021) and fainter than SN 2010ae (Stritzinger et al. 2014). Analysis of the bolometric light curve ($BgVri$, obtained through Superbol) of SN 2020kyg indicates that $\sim 0.002 \pm 0.001$ $M_\odot$ of ^{56}Ni was produced in the explosion.

Magee et al. (2016) suggested a correlation between the absolute magnitude, decline rate parameter, and rise time of

Table 7
References for Figures 17 and 18

SN	References
2002cx, 2003gq, 2004cs	Foley et al. (2013)
2005cc, 2008ae, 2009J, 2011ay	Foley et al. (2013)
2005hk	Stritzinger et al. (2015)
2007qd	McClelland et al. (2010)
2008A	Hicken et al. (2012),
	Foley et al. (2013)
2008ha	Foley et al. (2009),
	Foley et al. (2013)
2009ku	Narayan et al. (2011),
	Foley et al. (2013)
2010ae	Stritzinger et al. (2014)
2012Z	Stritzinger et al. (2015)
2014ck	Tomasella et al. (2016)
PS15csd	Magee et al. (2016)
PTF09ego, PTF09eoi, PTF11hyh	White et al. (2015)
2015H	Magee et al. (2016)
2019gsc	Srivastav et al. (2020),
	Tomasella et al. (2020)
2019muj	Barna et al. (2021)
2020sck	Dutta et al. (2022)
2020rea	Singh et al. (2022)
2021fcg	Karambelkar et al. (2021)
2018cni, 2020kyg	This work

Type Iax SNe in the R/r-band. Since then the sample has grown significantly, especially in the fainter end. An attempt is made to check for any possible correlation in the extended sample. Table 7 includes all the Type Iax SNe we have used in our study and their references. In Figure 17, we have plotted the absolute magnitude and decline rate parameter in the r/R-band for the extended sample. We have also included the N1-def, N3-def, and N5-def models (Fink et al. 2014) for comparison. We recover the weak correlation between the absolute magnitude and light-curve decline rate parameter as reported in Magee et al. (2016) and shown in Figure 17. However, dividing the current sample based on the brightness of the objects reveals an interesting trend: bright and faint objects behave differently. For the bright Type Iax cluster ($M_r \leqslant -17.1$ mag), there is a negative correlation with a correlation coefficient of 0.49 ($p = 0.044$), viz. the objects with a faster decline rate are found to be fainter. On the other hand, for the faint cluster ($M_r \geqslant -14.64$ mag), a trend of positive correlation emerges (Pearson correlation coefficient of -0.85, $p = 0.070$), viz. objects with a faster decline rate appear brighter. The sample of Type Iax studied so far is limited and a study with a bigger sample covering both the bright and faint end of luminosity distribution will be required to confirm this trend. In Figure 18, we have presented a plot between the rise time and absolute magnitude for a sample of well-studied Type Iax SNe. The rise times of SNe 2018cni and 2020kyg plotted in this figure are estimated from the spectral fitting (Section 5.2). From the plot, it is clear that the two quantities are correlated (Pearson correlation coefficient = -0.53, $p = 0.02$), the brighter objects tend to have a longer rise time. Type Iax SNe with fair premaximum coverage are included in this analysis, while some unfiltered measurements are not considered.

The spectral features of SNe 2018cni and 2020kyg appear similar, except for the Si II feature, which is prominent in SN 2020kyg. Modeling of the spectral sequence using TARDIS
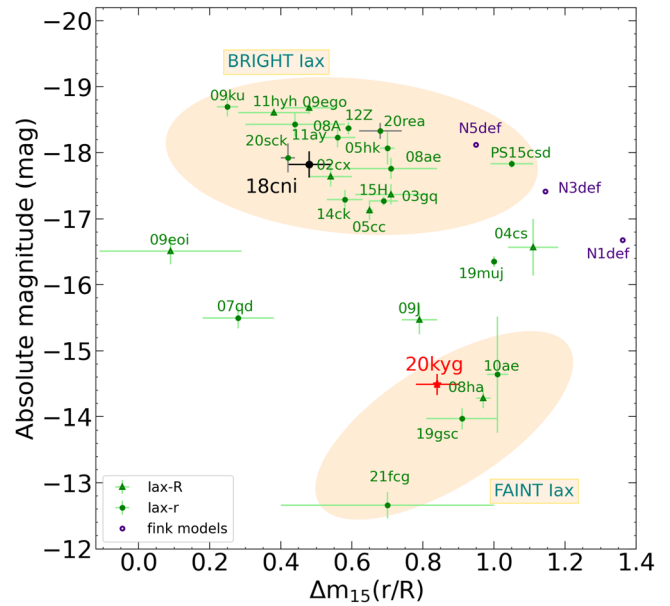
Figure 17. Absolute magnitude vs. light-curve decline rate in r/R-band for well-studied Type Iax SNe.
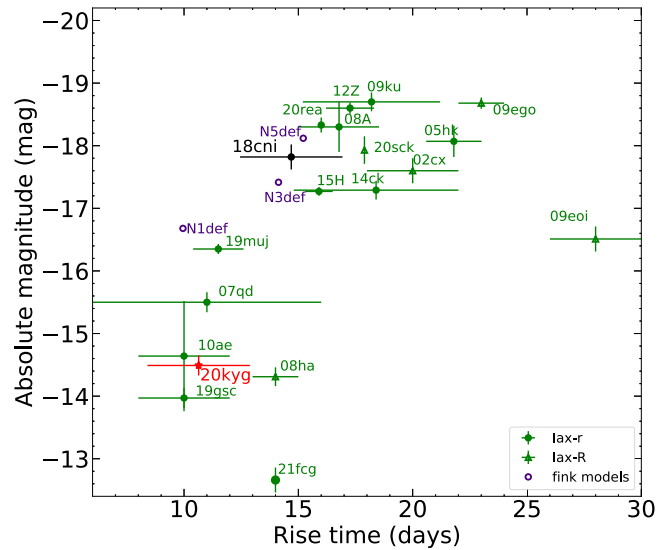
Figure 18. Distribution of Type Iax SNe in terms of the peak absolute magnitude and rise time in r/R-band. The figure clearly depicts the fact that Type Iax SNe follow a correlation in their peak luminosity and rise time.

indicates that some level of stratification at the outer layers and mixed ejecta in the inner layers are required.

Comparison of the bolometric light curves obtained through Superbol shows a resemblance of SN 2018cni with the N3-def model (Fink et al. 2014), whereas the luminosity of SN 2020kyg falls in the range of pure deflagration of a CONe white dwarf. For brighter members of the Type Iax class, several explosion scenarios have been proposed, such as pulsational-delayed detonation (Ivanova et al. 1974; Khokhlov 1991a, 1991b; Khokhlov et al. 1993; Hoeflich et al. 1995; Hoeflich & Khokhlov 1996; Bravo & García-Senz 2006; Baron et al. 2012; Dessart et al. 2014), deflagration-to-detonation transition (Khokhlov 1991a, 1991c; Khokhlov et al. 1993; Hoeflich et al. 1995; Hoeflich & Khokhlov 1996; Höflich et al. 2002; Seitenzahl et al. 2013; Sim et al. 2013),

pure deflagration of a white dwarf (Fink et al. 2014; Kromer et al. 2015), core-collapse origin (Foley et al. 2009, 2016; Valenti et al. 2009; Moriya et al. 2010), etc. Most of the observed properties of relatively bright Type Iax SNe match well with the predictions of pure deflagration of a white dwarf leaving behind a bound remnant. Observational properties of faint Type Iax can be explained by weak deflagration of a CONe white dwarf (Kromer et al. 2015), but the spectro-photometric evolution of these models is faster as compared to the observed ones. Another possible explanation is a double degenerate channel, which involves the merger of CO and ONe white dwarfs. This merger results in a failed detonation and is associated with a fast-declining transient (Kashyap et al. 2018) fainter than faint Type Iax SNe.

In any case, incomplete burning of the white dwarf explains most of the properties of Type Iax SNe, but the possibility for another progenitor scenario for faint members of this class cannot be ruled out completely. The different nature of the correlation between peak luminosity and light-curve decline rate for bright and faint members indicates heterogeneity within SNe Iax. Further study and in-depth analysis of this class will be required to understand their observed properties, progenitor system, and explosion mechanism.

ORCID iDs

Mridweeka Singh https://orcid.org/0000-0001-6706-2749
Devendra. K. Sahu https://orcid.org/0000-0002-6688-0800
Raya Dastidar https://orcid.org/0000-0001-6191-7160
Barnabás Barna https://orcid.org/0000-0003-4769-4794
Kuntal Misra https://orcid.org/0000-0003-1637-267X
Anjasha Gangopadhyay https://orcid.org/0000-0002-3884-5637
D. Andrew Howell https://orcid.org/0000-0003-4253-656X
Saurabh W. Jha https://orcid.org/0000-0001-8738-6011
Hyobin Im https://orcid.org/0000-0002-5742-8476
Kirsty Taggart https://orcid.org/0000-0002-5748-4558
Jennifer Andrews https://orcid.org/0000-0003-0123-0062
Daichi Hiramatsu https://orcid.org/0000-0002-1125-9187
Rishabh Singh Teja https://orcid.org/0000-0002-0525-0872
Craig Pellegrino https://orcid.org/0000-0002-7472-1279
Ryan J. Foley https://orcid.org/0000-0002-2445-5275
Arti Joshi https://orcid.org/0000-0001-9275-0287
G. C. Anupama https://orcid.org/0000-0003-3533-7183
K. Azalee Bostroem https://orcid.org/0000-0002-4924-444X
Jamison Burke https://orcid.org/0000-0003-0035-6659
Yssavo Camacho-Neves https://orcid.org/0000-0002-9830-3880
Lindsey A. Kwok https://orcid.org/0000-0003-3108-1328
Curtis McCully https://orcid.org/0000-0001-5807-7893
Yen-Chen Pan https://orcid.org/0000-0001-8415-6720
Matt Siebert https://orcid.org/0000-0003-2445-3891
Shubham Srivastav https://orcid.org/0000-0003-4524-6883
Tamás Szalai https://orcid.org/0000-0003-4610-1117
Jonathan J. Swift https://orcid.org/0000-0002-9486-818X
Grace Yang https://orcid.org/0000-0001-7823-2627
Henry Zhou https://orcid.org/0000-0002-2093-6960
Nico DiLullo https://orcid.org/0000-0003-4522-9653
Jackson Scheer https://orcid.org/0000-0002-3522-6312

References

Andrews, J. E., Sand, D. J., Valenti, S., et al. 2019, ApJ, 885, 43
Arnett, W. D. 1982, ApJ, 253, 785
Barna, B., Szalai, T., Jha, S. W., et al. 2021, MNRAS, 501, 1078
Barna, B., Szalai, T., Kerzendorf, W. E., et al. 2018, MNRAS, 480, 3609

Baron, E., Höflich, P., Krisciunas, K., et al. 2012, ApJ, 753, 105
Bobrick, A., Zenati, Y., Perets, H. B., Davies, M. B., & Church, R. 2022, MNRAS, 510, 3758
Bravo, E., & García-Senz, D. 2006, ApJL, 642, L157
Bravo, E., Gil-Pons, P., Gutiérrez, J. L., & Doherty, C. L. 2016, A&A, 589, A38
Brown, T. M., Baliber, N., Bianco, F. B., et al. 2013, PASP, 125, 1031
Cardelli, J. A., Clayton, G. C., & Mathis, J. S. 1989, ApJ, 345, 245
Crawford, S. M., Still, M., Schellart, P., et al. 2010, Proc. SPIE, 7737, 773725
Denissenkov, P. A., Truran, J. W., Herwig, F., et al. 2015, MNRAS, 447, 2696
Dessart, L., Blondin, S., Hillier, D. J., & Khokhlov, A. 2014, MNRAS, 441, 532
Dutta, A., Sahu, D. K., Anupama, G. C., et al. 2022, ApJ, 925, 217
Filippenko, A. V. 1982, PASP, 94, 715
Fink, M., Kromer, M., Seitenzahl, I. R., et al. 2014, MNRAS, 438, 1762
Foley, R. J., Brown, P. J., Rest, A., et al. 2010, ApJL, 708, L61
Foley, R. J., Challis, P. J., Chornock, R., et al. 2013, ApJ, 767, 57
Foley, R. J., Chornock, R., Filippenko, A. V., et al. 2009, AJ, 138, 376
Foley, R. J., Jha, S. W., Pan, Y.-C., et al. 2016, MNRAS, 461, 433
Foley, R. J., McCully, C., Jha, S. W., et al. 2014, ApJ, 792, 29
Guevel, D., & Hosseinzadeh, G. 2017, dguevel/PyZOGY: Initial Release, v0.0.1, Zenodo, doi:10.5281/zenodo.1043973
Hachinger, S., Mazzali, P. A., & Benetti, S. 2006, MNRAS, 370, 299
Hicken, M., Challis, P., Kirshner, R. P., et al. 2012, ApJS, 200, 12
Hiramatsu, D., Arcavi, I., Burke, J., et al. 2020, TNSCR, 2020-1559, 1
Hoeflich, P., & Khokhlov, A. 1996, ApJ, 457, 500
Hoeflich, P., Khokhlov, A. M., & Wheeler, J. C. 1995, ApJ, 444, 831
Höflich, P., Gerardy, C. L., Fesen, R. A., & Sakai, S. 2002, ApJ, 568, 791
Hoyle, F., & Fowler, W. A. 1960, ApJ, 132, 565
Ivanova, L. N., Imshennik, V. S., & Chechetkin, V. M. 1974, Ap&SS, 31, 497
Jha, S., Kirshner, R. P., Challis, P., et al. 2006, AJ, 131, 527
Jha, S. W. 2017, in Handbook of Supernovae, ed. A. W. Alsabti & P. Murdin (Berlin: Springer), 375
Jha, S. W., Maguire, K., & Sullivan, M. 2019, NatAs, 3, 706
Jordan, G. C., IV, Perets, H. B., Fisher, R. T., & van Rossum, D. R. 2012, ApJL, 761, L23
Jordi, K., Grebel, E. K., & Ammon, K. 2006, A&A, 460, 339
Karambelkar, V. R., Kasliwal, M. M., Maguire, K., et al. 2021, ApJL, 921, L6
Kashyap, R., Haque, T., Lorén-Aguilar, P., García-Berro, E., & Fisher, R. 2018, ApJ, 869, 140
Kawabata, M., Maeda, K., Yamanaka, M., et al. 2021, PASJ, 73, 1295
Kerzendorf, W., Nöbauer, U., Sim, S., et al. 2018, tardis-sn/tardis: TARDIS v2.0.2 release, Zenodo, doi:10.5281/zenodo.1292315
Kerzendorf, W., Nöbauer, U., Sim, S., et al. 2019, tardis-sn/tardis: TARDIS v3.0 alpha2, Zenodo, doi:10.5281/zenodo.2590539
Kerzendorf, W. E., & Sim, S. A. 2014, MNRAS, 440, 387
Khokhlov, A., Mueller, E., & Hoeflich, P. 1993, A&A, 270, 223
Khokhlov, A. M. 1991a, A&A, 245, L25
Khokhlov, A. M. 1991b, A&A, 246, 383
Khokhlov, A. M. 1991c, A&A, 245, 114
Kromer, M., Fink, M., Stanishev, V., et al. 2013, MNRAS, 429, 2287
Kromer, M., Ohlmann, S. T., Pakmor, R., et al. 2015, MNRAS, 450, 3045

Lach, F., Callan, F. P., Bubeck, D., et al. 2022, A&A, 658, A179
Li, W., Filippenko, A. V., Chornock, R., et al. 2003, PASP, 115, 453
Maeda, K., & Terada, Y. 2016, IJMPD, 25, 1630024
Magee, M. R., Gillanders, J. H., Maguire, K., Sim, S. A., & Callan, F. P. 2022, MNRAS, 509, 3580
Magee, M. R., Kotak, R., Sim, S. A., et al. 2016, A&A, 589, A89
Maoz, D., Mannucci, F., & Nelemans, G. 2014, ARA&A, 52, 107
McClelland, C. M., Garnavich, P. M., Galbany, L., et al. 2010, ApJ, 720, 704
McCully, C., Jha, S. W., Foley, R. J., et al. 2014a, Natur, 512, 54
McCully, C., Jha, S. W., Foley, R. J., et al. 2014b, ApJ, 786, 134
McCully, C., Jha, S. W., Scalzo, R. A., et al. 2022, ApJ, 925, 138
Meng, X., & Podsiadlowski, P. 2014, ApJL, 789, L45
Miller, J. S., & Stone, R. P. S. 1993, Lick Obs. Tech. Rep. 66, Lick Observatory
Moriya, T., Tominaga, N., Tanaka, M., et al. 2010, ApJ, 719, 1445
Narayan, G., Foley, R. J., Berger, E., et al. 2011, ApJL, 731, L11
Nicholl, M. 2018, RNAAS, 2, 230
Ochner, P., Pastorello, A., Cappellaro, E., et al. 2020, ATel, 13761, 1
Phillips, M. M. 1993, ApJL, 413, L105
Phillips, M. M., Li, W., Frieman, J. A., et al. 2007, PASP, 119, 360
Phillips, M. M., Lira, P., Suntzeff, N. B., et al. 1999, AJ, 118, 1766
Pumo, M. L., Turatto, M., Botticella, M. T., et al. 2009, ApJL, 705, L138
Sahu, D. K., Tanaka, M., Anupama, G. C., et al. 2008, ApJ, 680, 580
Schlafly, E. F., & Finkbeiner, D. P. 2011, ApJ, 737, 103
Seitenzahl, I. R., Ciaraldi-Schoolmann, F., Röpke, F. K., et al. 2013, MNRAS, 429, 1156
Siebert, M. R., Foley, R. J., Jones, D. O., et al. 2019, MNRAS, 486, 5785
Silverman, J. M., Vinkó, J., Marion, G. H., et al. 2015, MNRAS, 451, 1973
Sim, S. A., Seitenzahl, I. R., Kromer, M., et al. 2013, MNRAS, 436, 333
Singh, M., Misra, K., Sahu, D. K., et al. 2018, MNRAS, 474, 2551
Singh, M., Misra, K., Sahu, D. K., et al. 2022, MNRAS, 517, 5617
Smith, K. W., Srivastav, S., McBrien, O., et al. 2020, TNSAN, 113, 1
Srivastav, S., Smartt, S. J., Huber, M. E., et al. 2022, MNRAS, 511, 2708
Srivastav, S., Smartt, S. J., Leloudas, G., et al. 2020, ApJL, 892, L24
Stritzinger, M. D., Hsiao, E., Valenti, S., et al. 2014, A&A, 561, A146
Stritzinger, M. D., Valenti, S., Hoeflich, P., et al. 2015, A&A, 573, A2
Tan, H., Li, W., Li, B., et al. 2018, TNSTR, 2018-820, 1
Taubenberger, S. 2017, in Handbook of Supernovae, ed. A. W. Alsabti & P. Murdin (Berlin: Springer), 317
Tomasella, L., Cappellaro, E., Benetti, S., et al. 2016, MNRAS, 459, 1018
Tomasella, L., Stritzinger, M., Benetti, S., et al. 2020, MNRAS, 496, 1132
Tonry, J., Denneau, L., Heinze, A., et al. 2020, TNSTR, 2020-1539, 1
Tonry, J. L., Denneau, L., Heinze, A. N., et al. 2018, PASP, 130, 064505
Valenti, S., Benetti, S., Cappellaro, E., et al. 2008, MNRAS, 383, 1485
Valenti, S., Howell, D. A., Stritzinger, M. D., et al. 2016, MNRAS, 459, 3939
Valenti, S., Pastorello, A., Cappellaro, E., et al. 2009, Natur, 459, 674
Wang, B., & Han, Z. 2012, NewAR, 56, 122
White, C. J., Kasliwal, M. M., Nugent, P. E., et al. 2015, ApJ, 799, 52
Yamanaka, M., Maeda, K., Kawabata, K. S., et al. 2015, ApJ, 806, 191
Yaron, O., & Gal-Yam, A. 2012, PASP, 124, 668
Zhang, J., Tan, H., Li, W., et al. 2018a, ATel, 11728, 1
Zhang, J., Tan, H., Li, W., et al. 2018b, TNSCR, 2018-846, 1